minerals

MDPI

Structure and Behavior of the Ni End-Member Schreibersite Ni₃P under Compression to 50 GPa

Sasithorn Chornkrathok [1,2,*], Dongzhou Zhang [2] and Przemyslaw Dera [2]

[1] Department of Earth Sciences, University of Hawai'i at Mānoa, Honolulu, HI 96822, USA
[2] Hawai'i Institute of Geophysics and Planetology, University of Hawai'i at Mānoa, Honolulu, HI 96822, USA;
dzhang@hawaii.edu (D.Z.); pdera@hawaii.edu (P.D.)
* Correspondence: cs65@hawaii.edu; Tel.: +1-808-476-9793

check for
updates

Abstract: To better understand the potential presence of light element alloys of Fe and Ni in the Earth's interior, the crystal structure and compressional behavior of the Ni-P binary compound, schreibersite (Ni₃P), have been investigated using synchrotron X-ray diffraction experiments. Both powder and two single-crystal samples of synthetic Ni₃P (in different orientations with respect to the loading axis of the diamond anvil cell) were compressed up to approximately 50 GPa at ambient temperature. The compressional data obtained for Ni₃P were fitted with a 3rd order Birch–Murnaghan equation of state. All data indicated that the c/a ratio of unit cell parameters remained approximately constant up to about 30 GPa but then increased progressively with pressure, exhibiting a second slight discontinuity at approximately 40 GPa. The changes in unit cell parameters at ~30 GPa and ~40 GPa suggested discontinuous changes in magnetic ordering. Moreover, the threshold of these subtle discontinuities is sensitive to the stress state and orientation of the crystal in the diamond anvil cell. This study is the first report on the compressional behavior of both powder and single-crystal schreibersite at high-pressure (up to 50 GPa). It offers insights into the effects of Ni₃P components on the compressional behavior of the Earth's core.

Keywords: schreibersite; high pressure; diamond anvil cell; synchrotron x-ray diffraction; single-crystal x-ray diffraction

1. Introduction

Knowledge of the chemical composition and physical properties of the Earth's interior comes mostly from seismic observations, geophysical modeling, direct observation of surface rocks, and the study of meteorites [1–3]. Unfortunately, at present, Earth's deep interior cannot be directly sampled due to engineering limitations, as the deepest hole that has been drilled thus far reached only approximately 12 km [4]. Consequently, experimental investigations at high pressures and high temperatures have played an essential role in studying the Earth's interior. The Earth's core is believed to be comprised primarily of an iron-nickel (Fe-Ni) alloy. Still, a light element (sulfur, phosphorus, oxygen, etc.) component appears to be required as well, based upon current models and observations [1–3,5]. From seismic evidence, we know that the density of Earth's core is approximately 10% lower than that of pure Fe at the estimated core pressure and temperature [2,5,6]. The current interpretation of this density deficit involves the presence of a significant amount of nickel, along with small amounts (up to 10%) of one or more light elements such as sulfur, phosphorus, oxygen, silicon, hydrogen, carbon, and potassium [1,3,7]. In addition to reducing the density, the presence of light elements in Fe-Ni alloys also affects the elastic properties and acoustic wave velocities of the core. For example, alloying of Fe with silicon increases both the compressional and shear wave velocities, whereas adding Ni decreases the compressional and shear wave velocities [8]. To better

understand the evolution and formation of the Earth's core in terms of discrete material properties, experimentally measured elasticity and other physical parameters of potential alloys present in the Earth's core are required.

Among light elements suspected to be present in the core, phosphorus (P) is particularly interesting, because of its importance for life. P is present in the structure of living cells, helps to carry genetic information, is part of DNA, the fundamental building blocks of life, and contributes to adenosine triphosphate (ATP), the energy currency of life [9,10]. Although estimated concentration of P in the core is rather low (~0.2%) [3,11], phosphide minerals, especially Fe-Ni-P alloys that are found in iron-meteorites, such as iron monophosphide (FeP) [12,13], nickel monophosphide (NiP) [14], allabogdanite (($Fe, Ni)_2P$ (orthorhombic)) [15], barringerite (($Fe, Ni)_2P$ (hexagonal)) [16–18], schreibersite (($Fe, Ni)_3P$ (tetragonal)) [19–21], nickel-phosphide (($Ni, Fe)_3P$ (tetragonal)) [22,23], or melliniite (($Ni, Fe)_4P$) [24], have long been studied to understand the formation of planetary bodies.

Natural schreibersite (($Fe, Ni)_3P$), occurs as a minor phase in iron and stony-iron meteorites [19], where it usually shows a higher Fe than Ni content. Compositions with Ni content greater than 50% are called nickel phosphide [23]. Schreibersite has a metallic luster, a density of 7.0–7.3 g/cm^3, and hardness of 6.5–7 on the Mohs scale. It forms tetragonal crystals with perfect 001 cleavage and non-centrosymmetric space group I-4 [25]. In the schreibersite unit cell, there are four atomic positions in crystallographically non-equivalent 8g Wyckoff sites. Three of these are occupied by a metallic atom (Fe, Ni), while the fourth holds the P atom [25,26]. Although occurrences of schreibersite on the Earth's surface are rare, the implications of the possible presence of schreibersite in the deep interior might be important for the origin of life on Earth [10]. It is believed that meteoritic phosphide minerals, including schreibersite, could have been one of the primary sources of phosphorus on the early Earth [27,28]. Moreover, the concentration of phosphorus has a strong effect on the melting temperature in the Fe-P-S system [13].

The synthesis of minerals using high-pressure and temperature experimental techniques has given us insight into how these materials respond to the external forces that act on rocks at depth. Numerous previous studies have looked at alloys of Fe, Ni, and various light elements. Still, this research has focused primarily on Fe-rich compounds because Fe is the major component in the core. Pure Fe is stable in a hexagonal close-packed (hcp) crystal structure above ~10 GPa at 300 K [29,30], while pure Ni is stable in a face-centered cubic (fcc) structure at high pressure [31–33]. Alloying between iron and nickel leads to the stabilization of the fcc phase at high pressure and low temperature [30,32,33]. Another observation is that the value of the axial ratio (c/a) of the hcp-Fe phase is lower than the theoretical estimate. This has an effect on the longitudinal anisotropy of the hcp phase and might influence the seismic anisotropy of the Earth's core [32,34].

The possibility of forming alloys and solid compounds between Fe and light elements has stimulated a range of experimental studies that consider the stability, physical properties, and behavior of such phases, including schreibersite Fe end-member, Fe_3P, [19,35], as well as the isostructural Fe_3S [36–39]. Intriguing discontinuous behavior has been reported in Fe_3P, including, for example, a change in its c/a ratio on compression, attributed to changes in magnetic ordering [35]. A non-quenchable high-temperature phase of Fe_3P was discovered above 1600 K at 64 GPa [35]. The isostructural Fe_3S, is stable up to 220 GPa and 3300 K [39]. However, it also undergoes a magnetic collapse at 21 GPa, with the disordered magnetic moment affecting the elasticity and thermodynamics of this phase [36].

The Earth's core mainly consists of Fe, but the effects of Ni, the second major element, may also be significant, although they have not been investigated systematically. Constraining the properties of the Ni end-member of schreibersite is essential for understanding schreibersite's reactivity. It is crucial for proper modeling of solid solution phases with intermediate Fe/Ni ratios consistent with observations from meteorites. Thus, this investigation focuses on the study of the crystal structure and behavior of Ni end-member schreibersite (Ni_3P), specifically its crystal structure, at high pressures using synchrotron powder x-ray diffraction and synchrotron single-crystal X-ray diffraction.

2. Materials and Methods

2.1. Single Crystal X-Ray Diffraction at Ambient Conditions

The Ni_3P compound used in all our studies was synthesized by Dr. Nabil Boctor, at the Carnegie Institution for Science, from a stoichiometric mixture of elemental Ni and P in a molar ratio of 3:1, fused in a silica tube at 1000 °C and 1 atm in a high-temperature furnace. Ambient pressure measurements were conducted at the University of Hawai'i at Manoa X-ray Atlas Diffraction Laboratory, using a Bruker D8 Venture single crystal diffractometer equipped with a PHOTON-II CPAD detector and an Ag kα IµS microfocus source (0.56089 Å) Hawai'i. A synthetic single-crystal approximately $0.10 \times 0.08 \times 0.02$ mm in size was mounted on a Kapton loop and then aligned with the center of the instrument using a goniometer head. The data collection was conducted using APEX3 software (Version 2018.1-0, Bruker AXS Inc., Madison, WI, USA) [40]. The atomic positions, bond lengths, and angles were determined with the SHELXL program (Version 2018, Göttingen, Germany) [41].

2.2. High-Pressure X-Ray Diffraction

High-pressure single-crystal X-ray diffraction experiments were conducted at beamline 13BM-C of Advanced Photon Source (APS), Argonne National Laboratory. Two separate experiments were performed on the synthetic Ni_3P. Experiment 1 used synchrotron powder X-ray diffraction. Finely ground powder of Ni_3P was loaded into the diamond anvil cell with 0.300 mm culet-size standard diamonds mounted on asymmetric backing plates (cubic boron nitride towards the X-ray source and tungsten carbide towards the detector). A piece of Re metal foil with an initial thickness of 0.255 mm was pre-indented to 0.039 mm. The sample chamber was made by drilling a 0.180 mm diameter, laser-cut hole in the pre-indented gasket. A piece of gold foil and a ruby sphere were placed in the sample chamber, next to the sample for pressure calibration [42–44]. The diamond anvil cell (DAC) was loaded to ~0.5 GPa with neon as a pressure medium using the GSECARS/COMPRES gas loading system [45]. A monochromatic incident beam with a wavelength of 0.434 Å (28.6 keV) was used. The incident beam was focused to a spot of approximately 0.015 by 0.015 mm with a pair of Kirkpatrick–Baez mirrors. A MAR165 charge-coupled device (CCD, Rayonix L.L.C, Evanston, IL, USA) detector for recording the diffraction images was placed approximately 180 mm from the sample. Lanthanum hexaboride (LaB_6) powder was used to calibrate the distance and the tilting of the detector. The total angular opening of the DAC was ±12°. The sample was kept motionless during the exposure, with a typical exposure time of 5 s. The data were integrated and converted to 1-dimensional diffraction patterns using the Dioptas program [46].

Experiment 2 employed the synchrotron single-crystal x-ray diffraction technique. Two synthetic single-crystals of Ni_3P, C1, and C2, with approximate sizes of $0.040 \times 0.025 \times 0.005$ mm and $0.020 \times 0.020 \times 0.005$ mm, respectively, were loaded into the DAC with standard diamonds (0.300 mm cutlets). The diamond anvils were mounted on asymmetric backing plates (cubic boron nitride towards the X-ray source and tungsten carbide towards the detector). Crystal C1 was oriented with the (001) direction perpendicular to the diamond's cutlet, and C2 was oriented with the (001) parallel to the cutlet. The Re metal foil with an initial thickness of 0.255 mm was pre-indented to 0.045 mm, and the sample chamber was prepared by laser-cutting a 0.180 mm diameter hole in the pre-indented gasket using laser cutting. Gold foil and two ruby spheres were placed in the sample chamber, next to the samples for pressure calibration [42–44]. The DAC was loaded to ~0.5 GPa with neon as a pressure medium using the GSECARS/COMPRES gas loading system [45]. The characteristics of the beam and the instrument in experiment 2 were the same as in experiment 1. The total angular range (φ) covered during the scans ranged from 57 to 123° (with a total angular opening of ±33°). A series of step and wide-step φ-exposures were collected. Step scans involved 1° angular increments, and wide-step scans used 9.8° angular increments. The sample was rotated at a constant speed during the exposure, with a typical exposure time of 1s/deg. The single-crystal X-ray diffraction data were analyzed with

GSE_ADA and Reciprocal Space Viewer (RSV), as described in Reference [47]. The refinement of the crystal structure was done using the program SHELXL [41].

3. Results

3.1. Single Crystal X-Ray Diffraction at Ambient Conditions

The unit cell parameters of the Ni end-member schreibersite (Ni_3P) measured in our single-crystal X-ray diffraction experiment at ambient pressure. The measurements were as follows: a = 8.9515(2) Å, c = 4.3859(1) Å, and V_0 = 351.44(8) $Å^3$, consistent with the tetragonal structure with I-4 space group [48–50]. The fractional atomic coordinates and interatomic distances (bonding distances) in Ni_3P at ambient pressure are summarized in Tables 1 and 2, respectively. The structure of Ni_3P determined in this experiment is shown in Figure 1. The final figure of merit of the structure refinement, R1 obtained in this experiment, was 0.0239.

Table 1. Fractional atomic coordinates of Ni_3P at ambient pressure and temperature (numbers in parentheses represent errors in the last digit).

Element	x	y	z
Ni	0.9228(1)	0.8887(1)	0.7608(1)
Ni	0.6353(1)	0.9675(1)	0.0219(1)
Ni	0.8313(1)	0.7802(1)	0.2458(1)
P	0.7139(1)	0.9517(1)	0.5192(2)

Table 2. Bonding interatomic distances in Ni_3P at ambient pressure and temperature.

| Atom pair	Interatomic Distance (Å)
Ni_I–Ni_I	2.425(1), 2.710(1) × 2, 2.859(1)
Ni_I–Ni_{II}	2.649(1)
Ni_I–Ni_{III}	2.478(1), 2.592(1), 2.708(1), 2.732(1), 2.813(1)
Ni_{II}–Ni_{II}	2.491(1), 2.669(1), 2.669(1)
Ni_{II}–Ni_{III}	2.511(1), 2.544(1), 2.618(1)
Ni_{III}–Ni_{III}	2.687(1), 2.687(1)
Ni_I–P	2.222(1), 2.284(1)
Ni_{II}–P	2.296(1), 2.317(1), 2.318(1), 2.345(1)
Ni_{III}–P	2.214(1), 2.278(1), 2.337 (1)
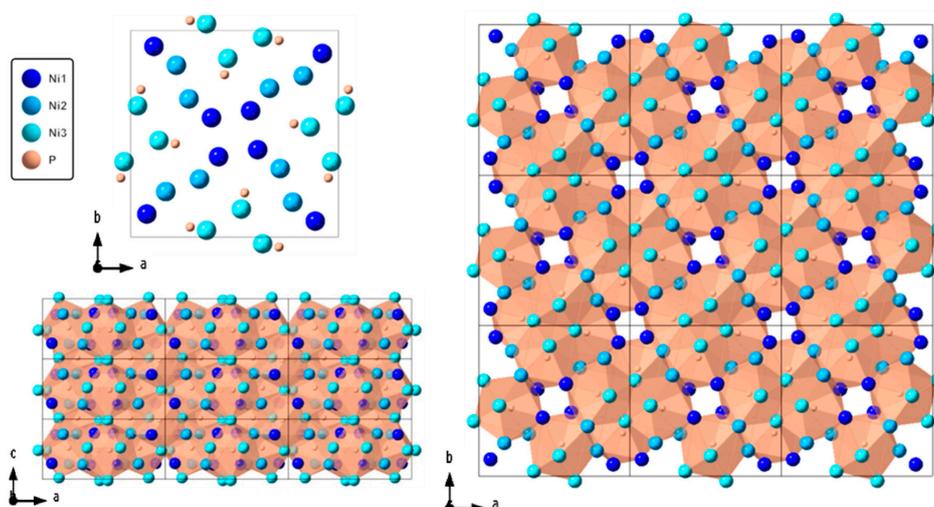
Figure 1. The crystal structure of Ni_3P at ambient pressure and temperature.

3.2. High-Pressure X-Ray Diffraction

The powder experiment was conducted in the pressure range of 0.5–46.0 GPa at ambient temperature. The unit cell parameters obtained from the powder data at the first pressure point are a = 8.945(1) Å, and c = 4.381(1) Å, consistent with the tetragonal structure. The crystal structure of Ni_3P remained tetragonal on compression to 46.0 GPa (Table 3). The ratio of the unit cell parameters (c/a) as a function of pressure remained constant with minor scatter around 0.4897(1) below 35.0 GPa. Above 35.0 GPa, the c/a ratio increased noticeably and approached 0.492(1) at 46.0 GPa (Figure 2). The normalized lattice parameters (a/a_0 and c/c_0) showed a decrease at a continuous rate for both parameters up to 46 GPa. Meanwhile, the slope of c changed discontinuously at 35 GPa (Figure 2), resulting in a change in the c/a ratio.

Table 3. Pressure dependence of the unit cell parameters of Ni_3P determined in the powder diffraction experiment.

Pressure (GPa)	a [Å]	c [Å]	Volume [A^3]
0.50(1)	8.945(1)	4.381(1)	350.5(1)
3.6(2)	8.901(1)	4.360(1)	345.5(1)
5.8(4)	8.874(1)	4.345(1)	342.2(1)
6.9(3)	8.853(4)	4.336(2)	339.9(4)
8.0(3)	8.842(1)	4.330(1)	338.5(1)
9.3(3)	8.824(1)	4.321(1)	336.5(1)
10.9 (4)	8.801(2)	4.311(2)	334.0(2)
12.9(5)	8.781(4)	4.301(4)	331.6(5)
15.0(5)	8.755(2)	4.288(2)	328.6(3)
16.5(5)	8.739(2)	4.280(1)	326.9(2)
19.0(5)	8.709(4)	4.267(3)	323.6(4)
21.5(5)	8.692(1)	4.257(1)	321.6(2)
21.8(1)	8.683(2)	4.253(1)	320.6(2)
24.0(4)	8.663(6)	4.242(3)	318.4(6)
25.8(4)	8.646(2)	4.233(2)	316.4(2)
27.7(4)	8.629(3)	4.225(2)	314.6(3)
29.5(5)	8.616(2)	4.218(1)	313.1(2)
31.9(5)	8.592(4)	4.207(3)	310.5(4)
33.4(4)	8.581(3)	4.200(1)	309.4(3)
35.2(3)	8.569(4)	4.194(2)	308.0(4)
36.6(4)	8.556(2)	4.189(2)	306.7(2)
38.5(4)	8.536(3)	4.180(1)	304.6(3)
41.0(2)	8.518(4)	4.174(3)	302.9(4)
42.2(2)	8.499(5)	4.170(3)	301.2(5)
44.1(1)	8.480(7)	4.165(5)	299.5(7)
46.0(2)	8.467(7)	4.163(7)	298.4(8)

The single crystal experiment was conducted over the pressure range 1.1–49.5 GPa at ambient temperature. Given the different orientation of the two sample crystals, the corresponding diffraction patterns were different, as shown in Figure 1. The unit cell parameters of the two samples are shown in Table 4. The unit cell parameters at 1.1 GPa confirmed that both single crystals were tetragonal, with a = 8.939(1) Å, and c = 4.378(2) Å for C1 and a = 8.936(1) Å, c = 4.375(1) Å for C2. Similar to the powder experiment, the c/a ratio was approximately constant at around 0.4899(3) below 30.0 GPa but started increasing significantly above that pressure, approaching 0.4928(4) at 49.5 GPa. For crystal C2, although the ratio of the cell parameter c/a below 25 GPa was constant at around 0.4897(2), it started to increase substantially above that pressure and reaches 0.4931(6) at 49.5 GPa, as shown in Figure 2. Moreover, between 40 and 45 GPa, both single crystals exhibited a slight change in the c/a ratio, which remained approximately constant at 0.4924(4). The normalized lattice parameters (a/a_0 and c/c_0) for the single crystal experiment revealed that there was a slight decrease in the slope of the c-axis at 30 GPa for C1 and 25 GPa for C2. This contributed to the change in the c/a ratio in both crystals, as shown in Figure 2.

Table 4. Pressure dependence of the unit cell parameters of Ni_3P determined in the single crystal experiment.

| Pressure (GPa)	Crystal	*a* [Å]	*c* [Å]	Volume [Å^3]
1.1(1)	C1	8.939(1)	4.378(2)	349.8(2)
	C2	8.936(1)	4.375(1)	349.4(1)
3.1(2)	C1	8.911(1)	4.363(1)	346.4(1)
	C2	8.906(1)	4.362(1)	346.0(1)
5.1(3)	C1	8.883(1)	4.350(2)	343.3(2)
	C2	8.876(1)	4.348(1)	342.6(1)
7.4(4)	C1	8.853(1)	4.334(2)	339.7(1)
	C2	8.851(1)	4.334(1)	339.5(1)
10.2(5)	C1	8.823(1)	4.321(1)	336.4(1)
	C2	8.819(1)	4.318(1)	335.8(1)
11.9(3)	C1	8.799(1)	4.309(2)	333.6(2)
	C2	8.797(1)	4.307(2)	333.3(2)
14.3(1)	C1	8.768(1)	4.294(2)	330.1(2)
	C2	8.767(1)	4.293(2)	330.0(1)
16.2(2)	C1	8.749(1)	4.286(3)	328.1(2)
	C2	8.745(1)	4.282(2)	327.5(2)
18.5(8)	C1	8.727(1)	4.276(2)	325.7(2)
	C2	8.721(1)	4.271(2)	324.9(2)
20.2(6)	C1	8.706(1)	4.266(2)	323.4(2)
	C2	8.702(1)	4.262(3)	322.8(2)
22.5(5)	C1	8.685(1)	4.256(3)	321.0(2)
	C2	8.677(1)	4.250(3)	319.9(2)
25.0(6)	C1	8.664(1)	4.244(3)	318.6(3)
	C2	8.655(1)	4.243(3)	317.8(3)
27.0(7)	C1	8.643(1)	4.235(3)	316.3(2)
	C2	8.634(2)	4.234(4)	315.7(3)
29.1(5)	C1	8.623(1)	4.226(4)	314.3(3)
	C2	8.608(2)	4.223(4)	312.9(3)
30.0(3)	C1	8.613(1)	4.224(3)	313.4(3)
	C2	8.599(2)	4.223(1)	311.0(1)
32.3(8)	C1	8.594(1)	4.220(4)	311.7(3)
	C2	8.581(2)	4.216(4)	310.4(3)
33.3(3)	C1	8.579(1)	4.215(4)	310.2(3)
	C2	8.568(2)	4.211(4)	309.1(3)
35.2(8)	C1	8.565(1)	4.212(4)	309.0(3)
	C2	8.551(2)	4.204(5)	307.5(3)
38.0(7)	C1	8.539(2)	4.200(5)	306.2(3)
	C2	8.521(2)	4.193(5)	304.5(4)
39.4(4)	C1	8.529(1)	4.197(4)	305.3(3)
	C2	8.514(2)	4.191(5)	303.8(4)
40.6(3)	C1	8.519(1)	4.193(3)	304.3(3)
	C2	8.501(2)	4.184(5)	302.4(4)
43.3(5)	C1	8.497(1)	4.184(3)	302.1(2)
	C2	8.473(2)	4.173(5)	299.6(4)
45.2(1)	C1	8.479(1)	4.174(3)	300.1(2)
	C2	8.460(2)	4.166(5)	298.2(4)
47.4(3)	C1	8.457(1)	4.164(3)	297.8(3)
	C2	8.440(2)	4.159(6)	296.3(4)
49.5(3)	C1	8.441(1)	4.160(4)	296.4(3)
	C2	8.427(3)	4.156(6)	295.1(4)
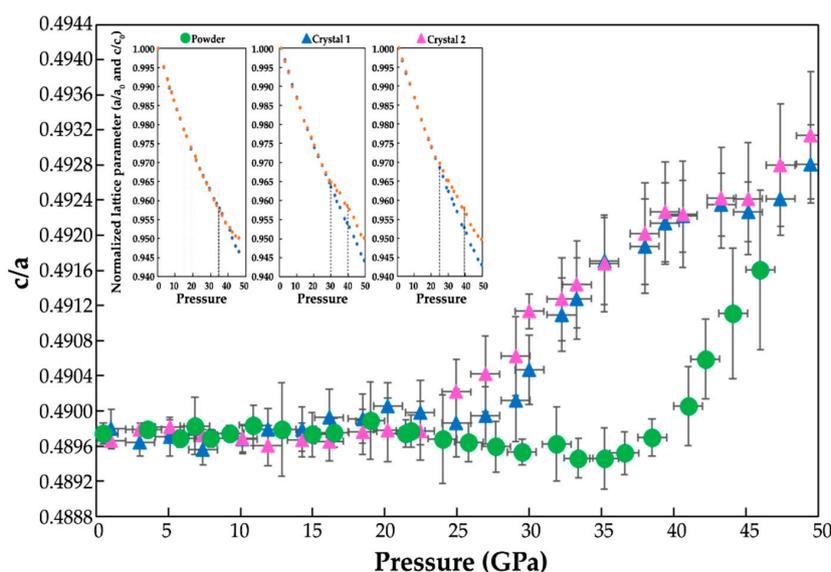
Figure 2. The c/a axial ratio of Ni_3P at different pressures at room temperature. The graphs at the top-left corner are the normalized lattice parameters (a/a_0 and c/c_0) of Ni_3P from this study.

The volume and pressure data from all experiments in this project were fit with a 3rd order Birch–Murnaghan equation of state (BM-EoS) using the EOS-FIT7 program [51]. Based on the independently-constrained value for the ambient unit cell volume (V_0 = 351.44(8) Å^3), for all data below the first transition of both powder and two single-crystal, the bulk modulus for schreibersite (K_{T0}) was 195(2) GPa and the first derivative of the bulk modulus (K_{T0}) was 4.5(2). The BM-EoS fit of powder data below 35 GPa yielded a bulk modulus of K_{T0} = 190(4) GPa, and its pressure derivative K'= 4.9(4). A discontinuity in incompressibility was observed at 35 GPa. For the single crystal experiment, the BM-EoS fit of C1 data below 30 GPa yielded the values K_{T0} = 199(5) GPa, K' = 4.7(4). Similarly, for C2, the volume data below 25 GPa were fit by 3rd BM-EoS, yielding K_{T0} = 194(5) GPa, K' = 4.7(8). The results of the BM-EoS fits in each sample are plotted in Figure 3. However, the data above the first discontinuity fit with the 2nd BM-EoS yielded V_0 = 352.22(2) Å^3, K_{T0} = 194(10) GPa.
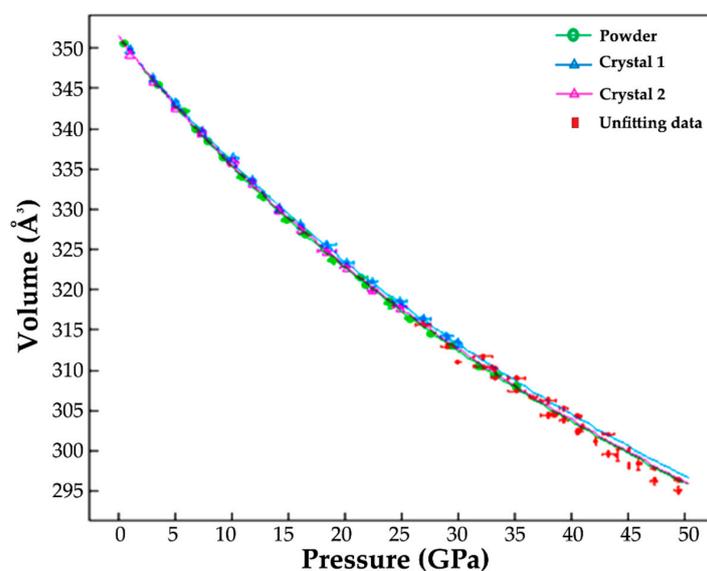

Figure 3. The volume-pressure curves represent the compression data of Ni_3P from high-pressure syn-XRD experiments.

The changes in bulk modulus as a function of pressure can be represented in the form of normalized pressure ($F = P(3f(1 + 2f)^{5/2}) - 1$) versus a Eulerian strain ($f = 0.5((V_0/V)^{2/3} - 1)$) plot [52]. The F-f plot from all data indicates $K' > 4$ (Figure 4). The linear character of all three F-f plots suggested that the second pressure derivative of the bulk modulus (K'') was negligible. EoS fit confidence ellipses are used for a visual assessment of the quality of the correlation between K_{T0} and K' (Figure 5). The confidence ellipses from all our data on Ni$_3$P are shown in Figure 5, drawn at a 95.4% confidence level (2σ), and it indicates that all calculated K_{T0} and K' values from this study are internally consistent.
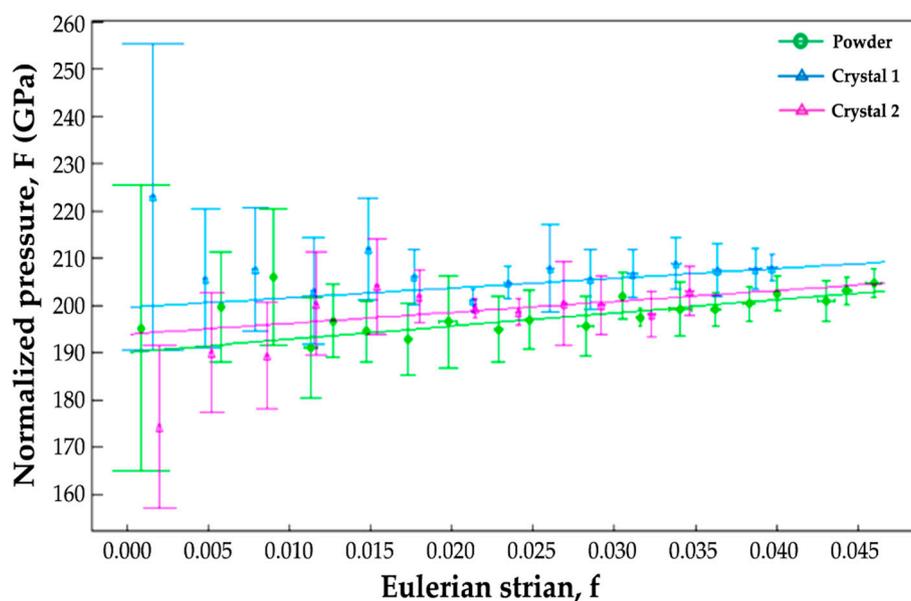
Figure 4. F-f plots for the Ni$_3$P compression below the first transition indicate that the second pressure derivative of the bulk modulus (K″) is negligible.
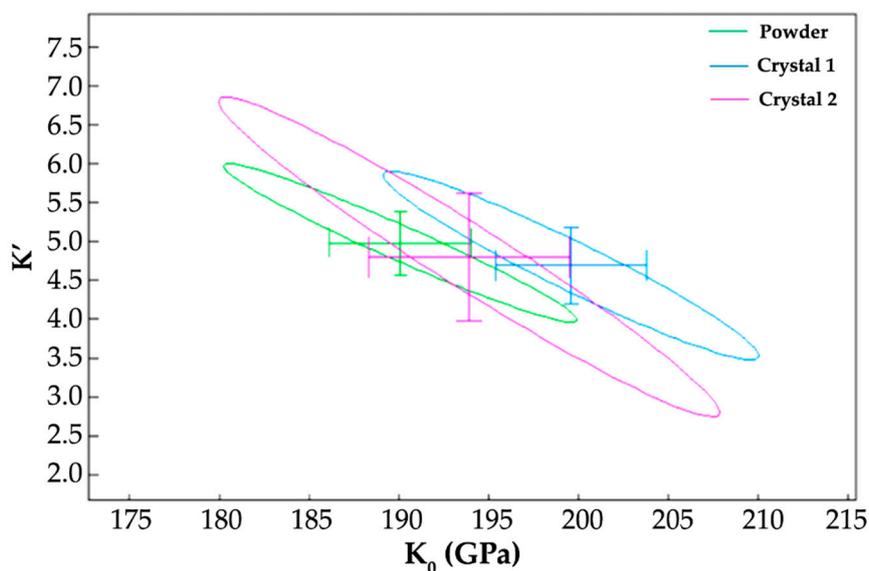
Figure 5. The confidence ellipses from all our data on Ni$_3$P are drawn at a 95.4% level, indicating that all calculated K_0 and K' values from this study are consistent.

4. Discussion

4.1. Crystal Structure at Ambient Condition.

The ambient unit cell parameters and interatomic distances of Ni_3P determined in this study are in good agreement with previous reports [48–50]. The atomic coordinates of Ni_3P determined in our single-crystal experiment represent the opposite absolute structure configuration of the mineral, which is a well-known phenomenon for molecules or crystals without a center of symmetry or mirror plane [53]. The space group of Ni_3P (I-4) does not include an inversion center (it is acentric). The fractional atomic coordinates from our experiments have been transformed to follow the convention used by previous studies [48–50]. However, despite differences in the absolute configuration, the structure of Ni_3P in this experiment is in excellent agreement with previously reported results.

4.2. Crystal Structure Evolution on Compression to 50 GPa

At ambient conditions, the unit cell parameters and volume of Ni_3P are slightly smaller than the ones of Fe_3P [19,35,54]. This shows that the unit cell parameters are controlled mainly by the cation size, as the ionic radius of nickel (~1.24 Å) is smaller than that of iron (~1.26 Å) [55].

In the powder sample, the c/a ratio starts to increase at 40 GPa; the same behavior is observed in single-crystal at 30 GPa in single crystal 1 and single-crystal 2 at 25 GPa (Figure 2). The experimental results indicate that the axial compressibility of Ni_3P is almost identical up to the transition point, above which the c-axis becomes less compressible. Differences in the transition pressure observed in the three experiments (powder, C1, and C2) indicate that the stress state and the orientation of the uniaxial stress component have a controlling effect over the transition point.

The sensitivity of some phase changes to uniaxial stress has been reported in the scientific literature. For example, first-principles calculations were used to predict the formation of a previously unknown high-pressure phase of SiO_2 with five-coordinated silicon that forms in response to stress applied to α-quartz, along a specific crystal orientation [56]. In SiO_2 α–cristobalite, two-phase changes to cristobalite II and cristobalite X-I are either observed [57] or suppressed [58] depending on the degree of hydrostaticity and stress rate. $CuGeO_3$ is one of the best-known examples of a material that is sensitive to uniaxial stress, with the ambient pressure phase going through two different series of phase changes depending on the degree of non-hydrosticity [59].

In the three comparative experiments conducted in this study, the pressure medium and stress fields were very similar (Ne). Neon is a good soft quasi-hydrostatic medium, but at pressures above 20 GPa, it starts displaying signs of uniaxial stress [60]. The three samples in our experiments were oriented in different ways in the stress field of the diamond anvil cell, which featured an enhanced uniaxial component aligned with the loading axis. The two single crystals had either the [100] or [001] directions exposed explicitly to the uniaxial stress. In contrast, in the powder samples, individual grains had all possible orientations to the uniaxial stress. We do not know the exact dependence of the phase change transition point on the direction of the uniaxial stress. It is hypothetically possible, for example, that the strongest effect would be associated with the [110] or [011] directions, rather than the principal directions [100] or [001]. The observed transition pressures for the two single crystals are both lower than the transition point observed for the powder sample. It is worth noting that the nature of the discontinuity in the single crystal and powder experiments was different. Single crystals seemed to transform through an immediate single-crystal to the single-crystal mechanism, with no evidence of two-phase coexistence. In the powder sample, there was most likely a two-phase coexistence with populations of differently oriented powder grains undergoing the phase change at different pressures, and relative phase fractions changing gradually. However, this effect was difficult to quantify, given the continuous nature of changes in the unit cell parameters.

Very similar effects observed in Fe_3P and Fe_3S have been attributed to changes in magnetic ordering [35,37,38]; therefore, we assume that the nature of the discontinuity in Ni_3P is of magnetic origin. However, we did not directly measure magnetic properties to provide direct proof of this

interpretation. We were also not able to conclusively verify the existence of the second transition due to the small number of pressure points collected above 40 GPa. Gu et al. [35] reported a magnetic collapse in Fe_3P around 40 GPa corresponding to a change of symmetry from I-4 to P4/mnc, based on first-principle calculations. The discontinuities in lattice parameters and volume as a function of pressure observed in our experiments at approximately 30 GPa and 40 GPa might be related to displacive phase changes. The change in the trend of the c/a ratio of Ni_3P in our experiments was also very similar to the magnetic transition and analogous c/a change observed in Cr_2O_3 [61,62]. The decreasing compressibility of the c-axis, contributing to the discontinuity in the c/a ratio trend, suggests that there are differences in the magnetic structure of schreibersite below and above the transition point [54].

The bulk modulus (K_{T0}) of Ni_3P from this experiment was in good agreement with the results of the first-principles calculations [63]. Moreover, the values of K_{T0} and K' of Ni_3P from our experiments were higher than values reported for isostructural compounds such as Fe_3P [19,35], Fe_3S [36–39], and Ni_3S [64]. This outcome suggested that the compressibility was controlled mainly by the cation size. Interestingly, K_{T0} and K' of Fe_3P and Fe_3S have quite similar values within the uncertainty, whereas K_{T0} and K' of Ni_3P are higher than Ni_3S. This indicates that changing the anion has a small effect on the compressibility behavior between Fe_3P and Fe_3S. However, the effect on the compressibility between Ni_3P and Ni_3S is stronger. The cause of the difference is that the synthetic Ni_3P in this paper was a stoichiometric compound, while Ni_3S in the earlier studies was non-stoichiometric. Moreover, the studies on Ni_3S were conducted only up to about 10 GPa, whereas we compressed our sample to approximately 50 GPa. If we focus only on the first 10 GPa of compressibility data, we also find that the trend of the c/a ratio of C1 is decreasing slightly over this range. Thus, to study the effect of the anion size between Ni_3P and Ni_3S, one might have to compress both samples to pressures higher than 10 GPa using samples as close to stoichiometric as possible.

4.3. Implications for Planetary Cores

To assess the effect the presence of Ni-rich schreibersite would have on the Earth's core, we compared the densities of pure iron, Fe_3P, and Ni_3P at pressures corresponding to the inner and outer core. It should be noted that these calculations were performed by extrapolating our results far beyond the range of conditions covered in our experiments based on a geothermal equation. The comparison showed that the density of Ni_3P from this experiment and Fe_3P from Gu et al. [35] was approximately 5% lower than the pure Fe at core pressure and ambient temperature. This result suggests that the presence of a significant amount of nickel and light elements such as phosphorus has the effect of lowering the density, consistent with the observed deficit in the density of the core as determined from seismic evidence [2,5,6]. Although our experiments did not include a study of the effects of high temperature on the unit cell parameter of Ni_3P, to a very simplified first approximation, we can compare the cold compressibility curves.

Gu et al., [35] argued that the discontinuities observed around 17 and 40 GPa were not only consistent with the calculated magnetic transitions but also probably produced discontinuous changes in the coefficient of thermal expansion. The thermal expansion coefficient $\alpha(p)$ decreases with increasing pressure. By analogy, we can assume that the compressional discontinuities observed in our experiments for Ni_3P at approximately 30 GPa and 40 GPa might also be related to discontinuities of thermal expansion and magnetic transitions. Thermal expansion decreases at high pressure, and with increasing bond energy, contributes to the high melting point. Therefore, at high pressure, most materials stay in the solid-state to much higher temperatures than at low pressure. At ambient pressure, Ni_3P has a melting point (~960 °C) lower than Fe_3P (~1100 °C) and pure iron (~1500 °C), which implies that addition of Ni_3P to natural schreibersite lowers the melting point [65–67].

The presence of Ni leads to loss of ferromagnetic order in Fe_3P because Ni causes a decrease of the magnetic moment [68,69]. Ni_3P is less compressible than pure hcp-Fe or iron phosphide phase, including Fe_3P [19,35]. Moreover, first-principles calculations on Ni_3P, Fe_3P, and pure hcp-Fe suggest

that the shear modulus of Ni_3P is lower than Fe_3P and pure hcp-Fe by approximately 30% and 20%, respectively [63,70,71]. The higher incompressibility and lower shear modulus of Ni_3P are consistent with the decrease of shear wave velocity of Fe under pressure when adding Ni to Fe-compounds [8].

5. Conclusions

The results of our diamond anvil cell experiments suggest that the volume and unit cell parameters of Ni_3P experience two discontinuities, at approximately 30 GPa and 40 GPa, which may be associated with corresponding magnetic transitions. The results of this study also illustrate that the transition c-axis of Ni_3P becomes less compressible than the a-axis. The discontinuity is sensitive to the stress state and orientation of the crystal in the diamond anvil cell. Moreover, the experiments suggest that substituting Ni into Fe-bearing compounds results in higher incompressibility of the mineral.

Further investigations of Fe-Ni alloys, including more direct measurements of their magnetic properties, are needed to explain the observed transitions fully more fully. Moreover, to reliably model core conditions, additional measurements will need to be conducted at a higher pressure and high temperature.

References

1. McDonough, W.F.; Sun, S.S. The composition of the Earth. *Chem. Geol.* **1995**, *120*, 223–253. [CrossRef]
2. Allègre, C.J.; Poirier, J.P.; Humler, E.; Hofmann, A.W. The chemical composition of the Earth. *Earth Planet. Sci. Lett.* **1995**, *134*, 515–526. [CrossRef]
3. Litasov, K.D.; Shatskiy, A.F. Composition of the Earth's core. *Russ. Geol. Geophys.* **2016**, *57*, 22–46. [CrossRef]
4. Kozlovsky, Y.A. The world's deepest well. *Sci. Am.* **1984**, *251*, 98–105. [CrossRef]
5. Birch, F. Elasticity and constitution of the Earth's interior. *J. Geophys. Res.* **1952**, *57*, 227–286. [CrossRef]
6. Li, J.; Fei, Y. Experimental constraints on core composition. *Treatise Geochem.* **2003**, *2*, 568.
7. Poirier, J.P. Light elements in the Earth's outer core: A critical review. *Phys. Earth Planet. Inter.* **1994**, *85*, 319–337. [CrossRef]
8. Lin, J.F.; Struzhkin, V.V.; Sturhahn, W.; Huang, E.; Zhao, J.; Hu, M.Y.; Alp, E.E.; Mao, H.K.; Boctor, N.; Hemley, R.J. Sound velocities of iron-nickel and iron-silicon alloys at high pressures. *Geophys. Res. Lett.* **2003**, *30*. [CrossRef]
9. Maciá, E.; Hernández, M.V.; Oró, J. Primary sources of phosphorus and phosphates in chemical evolution. *Orig. Life Evol. Biosph.* **1997**, *27*, 459–480. [CrossRef]
10. Bryant, D.E.; Greenfield, D.; Walshaw, R.D.; Johnson, B.R.; Herschy, B.; Smith, C.; Pasek, M.A.; Telford, R.; Scowen, I.; Munshi, T.; et al. Hydrothermal modification of the Sikhote-Alin iron meteorite under low pH geothermal environments. A plausibly prebiotic route to activated phosphorus on the early Earth. *Geochim. Cosmochim. Acta* **2013**, *109*, 90–112. [CrossRef]

11. McDonough, W.F. 3.16–Compositional model for the Earth's core. *Treatise Geochem (2nd edition).* **2014**, *3*, 559–577.

12. Gu, T.; Wu, X.; Qin, S.; Dubrovinsky, L. In situ high-pressure study of FeP: Implications for planetary cores. *Phys. Earth Planet. Inter.* **2011**, *184*, 154–159. [CrossRef]

13. Stewart, A.J.; Schmidt, M.W. Sulfur and phosphorus in the Earth's core: The Fe-P-S system at 23 GPa. *Geophys. Res. Lett.* **2007**, *34*. [CrossRef]

14. Dera, P.; Lazarz, J.D.; Lavina, B. Pressure-induced development of bonding in NiAs type compounds and polymorphism of NiP. *J. Solid State Chem.* **2011**, *184*, 1997–2003. [CrossRef]

15. Britvin, S.N.; Rudashevsky, N.S.; Krivovichev, S.V.; Burns, P.C.; Polekhovsky, Y.S. Allabogdanite, (Fe, Ni)$_2$P, a new mineral from the Onello meteorite: The occurrence and crystal structure. *Am. Mineral.* **2002**, *87*, 1245–1249. [CrossRef]

16. Brandstätter, F.; Koeberl, C.; Kurat, G. The discovery of iron barringerite in lunar meteorite Y-793274. *Geochim. Cosmochim. Acta* **1991**, *55*, 1173–1174. [CrossRef]

17. Buseck, P.R. Phosphide from meteorites: Barringerite, a new iron-nickel mineral. *Science* **1969**, *165*, 169–171. [CrossRef]

18. Dera, P.; Lavina, B.; Borkowski, L.A.; Prakapenka, V.B.; Sutton, S.R.; Rivers, M.L.; Downs, R.T.; Prewitt, C.T. Structure and behavior of the barringerite Ni end-member, Ni$_2$P, at deep Earth conditions and implications for natural Fe-Ni phosphides in planetary cores. *J. Geophys. Res. Solid Earth* **2009**, *114*. [CrossRef]

19. Geist, V.; Wagner, G.; Nolze, G.; Moretzki, O. Investigations of the meteoritic mineral (Fe, Ni)$_3$P. *Cryst. Res. Technol. J. Exp. Ind. Crystallogr.* **2005**, *40*, 52–64. [CrossRef]

20. Scott, H.P.; Huggins, S.; Frank, M.R.; Maglio, S.J.; Martin, C.D.; Meng, Y.; Santillán, J.; Williams, Q. Equation of state and high-pressure stability of Fe$_3$P -schreibersite: Implications for phosphorus storage in planetary cores. *Geophys. Res. Lett.* **2007**, *34*. [CrossRef]

21. He, X.J.; Guo, J.Z.; Wu, X.; Huang, S.X.; Qin, F.; Gu, X.P.; Qin, S. Compressibility of natural schreibersite up to 50 GPa. *Phys. Chem. Miner.* **2019**, *46*, 91–99. [CrossRef]

22. Britvin, S.N.; Kolomenskii, V.D.; Boldyreva, M.M.; Bogdanova, A.N.; Kretser, Y.L.; Boldyreva, O.N.; Rudashevskii, N.S. Nickelphosphide (Ni, Fe)$_3$P, the nickel analog of schreibersite. *ЗАПИСКИ РОССИЙСКОГО МИНЕРАЛОГИЧЕСКОГО ОБЩЕСТВА* **1999**, *128*, 64–72.

23. Skála, R.; Drábek, M. Nickelphosphide from the Vicenice octahedrite: Rietveld crystal structure refinement of synthetic analogue. *Mineral. Mag.* **2003**, *67*, 783–792. [CrossRef]

24. Pratesi, G.; Bindi, L.; Moggi-Cecchi, V. Icosahedral coordination of phosphorus in the crystal structure of melliniite, a new phosphide mineral from the Northwest Africa 1054 acapulcoite. *Am. Mineral.* **2006**, *91*, 451–454. [CrossRef]

25. Skála, R.; Císařová, I. Crystal structure of meteoritic schreibersite: Determination of absolute structure. *Phys. Chem. Miner.* **2005**, *31*, 721–732. [CrossRef]

26. Pritekel, C. The crystal structure of meteoritic schreibersite: Refinement of the absolute crystal structure. Bachelor's Thesis, University of Colorado Boulder, Boulder, CO, USA, January 2015.

27. Pasek, M.A.; Lauretta, D.S. Aqueous corrosion of phosphide minerals from iron meteorites: A highly reactive source of prebiotic phosphorus on the surface of the early Earth. *Astrobiology* **2005**, *5*, 515–535. [CrossRef]

28. Gull, M.; Mojica, M.A.; Fernández, F.M.; Gaul, D.A.; Orlando, T.M.; Liotta, C.L.; Pasek, M.A. Nucleoside phosphorylation by the mineral schreibersite. *Sci. Rep.* **2015**, *5*, 17198. [CrossRef]

29. Hemley, R.J.; Mao, H.K. In situ studies of iron under pressure: New windows on the Earth's core. *Int. Geol. Rev.* **2001**, *43*, 1–30.

30. Kuwayama, Y.; Hirose, K.; Sata, N.; Ohishi, Y. Phase relations of iron and iron–nickel alloys up to 300 GPa: Implications for composition and structure of the Earth's inner core. *Earth Planet. Sci. Lett.* **2008**, *273*, 379–385. [CrossRef]

31. Huang, E.; Bassett, W.A.; Weathers, M.S. Phase relationships in Fe-Ni alloys at high pressures and temperatures. *J. Geophys. Res. Solid Earth* **1988**, *93*, 7741–7746. [CrossRef]

32. Lin, J.F.; Heinz, D.L.; Campbell, A.J.; Devine, J.M.; Shen, G. Iron-silicon alloy in Earth's core? *Science* **2002**, *295*, 313–315. [CrossRef] [PubMed]

33. Mao, W.L.; Campbell, A.J.; Heinz, D.L.; Shen, G. Phase relations of Fe–Ni alloys at high pressure and temperature. *Phys. Earth Planet. Inter.* **2006**, *155*, 146–151. [CrossRef]

34. Steinle-Neumann, G.; Stixrude, L.; Cohen, R.E.; Gülseren, O. Elasticity of iron at the temperature of the Earth's inner core. *Nature* **2001**, *413*, 57. [CrossRef] [PubMed]

35. Gu, T.; Fei, Y.; Wu, X.; Qin, S. High-pressure behavior of Fe₃P and the role of phosphorus in planetary cores. *Earth Planet. Sci. Lett.* **2014**, *390*, 296–303. [CrossRef]

36. Fei, Y.; Li, J.; Bertka, C.M.; Prewitt, C.T. Structure type and bulk modulus of Fe₃S, a new iron-sulfur compound. *Am. Mineral.* **2000**, *85*, 1830–1833. [CrossRef]

37. Lin, J.F.; Fei, Y.; Sturhahn, W.; Zhao, J.; Mao, H.K.; Hemley, R.J. Magnetic transition and sound velocities of Fe₃S at high pressure: Implications for Earth and planetary cores. *Earth Planet. Sci. Lett.* **2004**, *226*, 33–40. [CrossRef]

38. Seagle, C.T.; Campbell, A.J.; Heinz, D.L.; Shen, G.; Prakapenka, V.B. Thermal equation of state of Fe₃S and implications for sulfur in Earth's core. *J. Geophys. Res. Solid Earth* **2006**, *111*. [CrossRef]

39. Kamada, S.; Terasaki, H.; Ohtani, E.; Sakai, T.; Kikegawa, T.; Ohishi, Y.; Hirao, N.; Sata, N.; Kondo, T. Phase relationships of the Fe-FeS system in conditions up to the Earth's outer core. *Earth Planet. Sci. Lett.* **2010**, *294*, 94–100. [CrossRef]

40. Bruker. *APEX3 Crystallography Software Suite*; Bruker AXS Inc.: Madison, WI, USA, 2016.

41. Sheldrick, G.M. A short history of SHELX. *Acta Crystallogr. Sect. A Found. Crystallogr.* **2008**, *64*, 112–122. [CrossRef]

42. Heinz, D.L.; Jeanloz, R. The equation of state of the gold calibration standard. *J. Appl. Phys.* **1984**, *55*, 885–893. [CrossRef]

43. Mao, H.K.; Bell, P.M.; Shaner, J.T.; Steinberg, D.J. Specific volume measurements of Cu, Mo, Pd, and Ag and calibration of the ruby R1 fluorescence pressure gauge from 0.06 to 1 Mbar. *J. Appl. Phys.* **1978**, *49*, 3276–3283. [CrossRef]

44. Mao, H.K.; Xu, J.A.; Bell, P.M. Calibration of the ruby pressure gauge to 800 kbar under quasi-hydrostatic conditions. *J. Geophys. Res. Solid Earth* **1986**, *91*, 4673–4676. [CrossRef]

45. Rivers, M.; Prakapenka, V.B.; Kubo, A.; Pullins, C.; Holl, C.M.; Jacobsen, S.D. The COMPRES/GSECARS gas-loading system for diamond anvil cells at the Advanced Photon Source. *High Press. Res.* **2008**, *28*, 273–292. [CrossRef]

46. Prescher, C.; Prakapenka, V.B. DIOPTAS: A program for reduction of two-dimensional X-ray diffraction data and data exploration. *High Press. Res.* **2015**, *35*, 223–230. [CrossRef]

47. Dera, P.; Zhuravlev, K.; Prakapenka, V.; Rivers, M.L.; Finkelstein, G.J.; Grubor-Urosevic, O.; Tschauner, O.; Clark, S.M.; Downs, R.T. High pressure single-crystal micro X-ray diffraction analysis with GSE_ADA/RSV software. *High Press. Res.* **2013**, *33*, 466–484. [CrossRef]

48. Aronsson, B. The crystal structure of Ni₃P.(Fe₃P-Type). *Acta Chem. Scand.* **1955**, *9*, 137–140. [CrossRef]

49. Rundqvist, S.; Hassler, E.; Lundvik, L. Refinement of Ni₃P Structure. *Acta Chem. Scand.* **1962**, *16*, 242.

50. Jun, R.E.N.; Wang, J.G.; Li, J.F.; Li, Y.W. Density functional theory study on crystal nickel phosphides. *J. Fuel Chem. Technol.* **2007**, *35*, 458–464.

51. Gonzalez-Platas, J.; Alvaro, M.; Nestola, F.; Angel, R. EosFit7-GUI: A new graphical user interface for equation of state calculations, analyses and teaching. *J. Appl. Crystallogr.* **2016**, *49*, 1377–1382. [CrossRef]

52. Birch, F. Finite strain isotherm and velocities for single-crystal and polycrystalline NaCl at high pressures and 300 K. *J. Geophys. Res. Solid Earth* **1978**, *83*, 1257–1268. [CrossRef]

53. Flack, H.D. Chiral and achiral crystal structures. *Helv. Chim. Acta* **2003**, *86*, 905–921. [CrossRef]

54. Howard, J.W. Finite strain studies of single crystal Fe₃P under high pressures. Master's Thesis, University of Nevada Las Vegas, Las Vegas, NV, USA, 2010.

55. Greenwood, N.N.; Earnshaw, A. *Chemistry of the Elements*; Elsevier: Oxford, UK, 2012.

56. Badro, J.; Teter, D.M.; Downs, R.T.; Gillet, P.; Hemley, R.J.; Barrat, J.L. Theoretical study of a five-coordinated silica polymorph. *Phys. Rev. B* **1997**, *56*, 5797. [CrossRef]

57. Dove, M.T.; Craig, M.S.; Keen, D.A.; Marshall, W.G.; Redfern, S.A.T.; Trachenko, K.O.; Tucker, M.G. Crystal structure of the high-pressure monoclinic phase-II of cristobalite, SiO₂. *Min. Mag.* **2000**, *64*, 569–576. [CrossRef]

58. Dera, P.; Lazarz, J.D.; Prakapenka, V.B.; Barkley, M.; Downs, R.T. New insights into the high-pressure polymorphism of SiO₂ cristobalite. *Phys. Chem. Miner.* **2011**, *38*, 517–529. [CrossRef]

59. Dera, P.; Jayaraman, A.; Prewitt, C.T.; Gramsch, S.A. Structural basis for high-pressure polymorphism in CuGeO₃. *Phys. Rev. B* **2002**, *65*, 134105. [CrossRef]

60. Klotz, S.; Chervin, J.C.; Munsch, P.; Le Marchand, G. Hydrostatic limits of 11 pressure transmitting media. *J. Phys. D Appl. Phys.* **2009**, *42*, 075413. [CrossRef]

61. Dera, P.; Lavina, B.; Meng, Y.; Prakapenka, V.B. Structural and electronic evolution of Cr_2O_3 on compression to 55 GPa. *J. Solid State Chem.* **2011**, *184*, 3040–3049. [CrossRef]

62. Golosova, N.O.; Kozlenko, D.P.; Kichanov, S.E.; Lukin, E.V.; Liermann, H.P.; Glazyrin, K.V.; Savenko, B.N. Structural and magnetic properties of Cr_2O_3 at high pressure. *J. Alloy. Compd.* **2017**, *722*, 593–598. [CrossRef]

63. Zhao, D.; Zhou, L.; Du, Y.; Wang, A.; Peng, Y.; Kong, Y.; Sha, C.; Ouyang, Y.; Zhang, W. Structure, elastic and thermodynamic properties of the Ni–P system from first-principles calculations. *Calphad* **2011**, *35*, 284–291. [CrossRef]

64. Urakawa, S.; Matsubara, R.; Katsura, T.; Watanabe, T.; Kikegawa, T. Stability and bulk modulus of Ni_3S, a new nickel sulfur compound, and the melting relations of the system Ni-NiS up to 10 GPa. *Am. Mineral.* **2011**, *96*, 558–565. [CrossRef]

65. Lyman, T. *Metallography, Structures and Phase Diagrams, Metal Handbook*; American Society for Metals: Metals Park, OH, USA, 1973.

66. Okamoto, H. Fe-P (Iron-Phosphorus). *J. Phase Equilibria Diffus.* **2007**, *28*, 588. [CrossRef]

67. Kim, T.Y.; Son, H.J.; Lim, S.K.; Song, Y.I.; Park, H.S.; Suh, S.J. Electroless Nickel Alloy Deposition on SiO_2 for Application as a Diffusion Barrier and Seed Layer in 3D Copper Interconnect Technology. *J. Nanosci. Nanotechnol.* **2014**, *14*, 9515–9524. [CrossRef] [PubMed]

68. Gambino, R.J.; McGuire, T.R.; Nakamura, Y. Magnetic Properties of the Iron-Group Metal Phosphides. *J. Appl. Phys.* **1967**, *38*, 1253–1255. [CrossRef]

69. Goto, M.; Tange, H.; Tokunaga, T.; Fujii, H.; Okamoto, T. Magnetic properties of the $(Fe_{1-x}M_x)_3P$ compounds. *Jpn. J. Appl. Phys.* **1977**, *16*, 2175. [CrossRef]

70. Li, L.H.; Wang, W.L.; Hu, L.; Wei, B.B. First-principle calculations of structural, elastic and thermodynamic properties of Fe–B compounds. *Intermetallics* **2014**, *46*, 211–221. [CrossRef]

71. Wu, J.; Chong, X.; Zhou, R.; Jiang, Y.; Feng, J. Structure, stability, mechanical and electronic properties of Fe–P binary compounds by first-principles calculations. *RSC Adv.* **2015**, *5*, 81943–81956. [CrossRef]